

Efficient Sparse Imaging Reconstruction Algorithm for Through-the-Wall Radar

Lele Qu*, Xing Cheng, and Tianhong Yang

Abstract—Sparse reconstruction technique can be used to provide high-resolution imaging result for through-the-wall radar (TWR) system. Since conventional sparse imaging reconstruction algorithms usually require a tremendous amount of computer memory and computational complexity, it is very difficult to apply in the practical large-scale TWR imaging applications. To solve the above problem, an efficient sparse imaging reconstruction algorithm is proposed in this paper. The proposed imaging method combines the spectral projection gradient L1-norm (SPGL1) algorithm with nonuniform fast Fourier transform (NUFFT) technique to achieve imaging reconstruction. Benefiting from the function handle operation of SPGL1 and computational efficiency of NUFFT, the proposed imaging algorithm can significantly reduce the memory requirement and computation complexity. The simulated and experimental results have shown that the proposed imaging method can significantly reduce the required computer memory and computational cost while providing the similar recovered image quality as the conventional sparse imaging method.

1. INTRODUCTION

Through-the-wall radar (TWR) imaging has drawn substantial attention due to its numerous civilian and military applications in surveillance, reconnaissance and rescue operations [1]. For these applications, it is crucial to design effective imaging algorithms to obtain clean and highly resolved image of a scene of interest behind an opaque obstacle. In most TWR imaging scenarios, a wideband waveform in conjunction with a large antenna aperture is required to achieve the highly resolved images. This results in a great amount of measurement data, long data acquisition time, as well as large storage and memory requirement. The compressive sensing (CS) and sparse reconstruction techniques have been successfully applied to TWR imaging for speeding up data acquisition and achieving high-resolution imaging. The first application of CS to TWR imaging was presented in [2] and further developed in [3–6]. In particular, a number of robust sparse TWR imaging algorithms have been proposed for hostile environments such as strong front wall clutter [7, 8] and multipath echo interference [9].

Although the existing sparse imaging approaches are capable of obtaining successful imaging results, these algorithms require that the data dictionary matrix should be explicitly constructed before the imaging process and thus are quite computationally intensive with huge memory burden, which typically make these algorithms impractical for large-scale TWR imaging problems. Therefore, in order to improve the efficiency both in terms of memory and computational complexity, an efficient sparse imaging reconstruction algorithm for TWR system is proposed in this paper. In the proposed imaging method, the spectral projection gradient L1-norm (SPGL1) algorithm [10] combined with nonuniform fast Fourier transform (NUFFT) technique [11] is employed to reduce the required computer memory and improve computational efficiency. Benefiting from the function handle operation of SPGL1 and computational efficiency of NUFFT, the proposed imaging algorithm can significantly reduce the

Received 22 April 2017, Accepted 11 July 2017, Scheduled 22 July 2017

* Corresponding author: Lele Qu (lele83.qu@gmail.com).

The authors are with the College of Electronic Information Engineering, Shenyang Aerospace University, Shenyang 110136, China.

memory requirement and accelerate the matrix-vector multiplication in the imaging reconstruction process.

The remainder of this paper is organized as follows. Section 2 outlines signal model of sparse TWR imaging problem. The proposed efficient sparse imaging reconstruction algorithm for TWR system is presented in Section 3. Experimental results are provided in Section 4 to validate the performance and efficiency of the proposed imaging approach. Section 5 concludes this paper.

2. SIGNAL MODEL

The TWR imaging problem is formulated assuming a stepped-frequency continuous-wave (SFCW) radar system. The scene of interest to be imaged is divided into Q pixels in crossrange and downrange. Consider an M -element line array of transceivers and N frequencies equispaced over the desired working bandwidth, the target return at the m th ($m = 0, \dots, M - 1$) antenna corresponding to the n th ($n = 0, \dots, N - 1$) frequency can be expressed as

$$r_m(n) = \sum_{q=0}^{Q-1} \sigma_q e^{-j2\pi f_n \tau_{m,q}} \quad (1)$$

where σ_q is the reflection coefficient corresponding to the q th pixel, which is assumed to be independent of frequency and transceiver location. $f_n = f_0 + n\Delta f$ is the n th working frequency, f_0 the starting frequency, Δf the uniform frequency step, and $\tau_{m,q}$ the round-trip propagation time between the m th antenna location and the q th pixel.

Vectoring the image of the investigated area into the $Q \times 1$ scene reflectivity vector $\boldsymbol{\sigma} = [\sigma_0, \sigma_1, \dots, \sigma_{Q-1}]^T$, the signal model of Eq. (1) can be expressed in an equivalent matrix-vector form as

$$\mathbf{r}_m = \boldsymbol{\Psi}_m \boldsymbol{\sigma} \quad (2)$$

where $\mathbf{r}_m = [r_m(0), \dots, r_m(1), \dots, r_m(N-1)]^T$ is the $N \times 1$ local measurement vector corresponding to the m th antenna location. $\boldsymbol{\Psi}_m$ is the $N \times Q$ local dictionary matrix, and its n th row is given by

$$[\boldsymbol{\Psi}_m]_n = [e^{-j2\pi f_n \tau_{m,0}}, e^{-j2\pi f_n \tau_{m,1}}, \dots, e^{-j2\pi f_n \tau_{m,Q-1}}] \quad (3)$$

Considering that there are total M available antenna locations, the TWR imaging model is described as

$$\mathbf{r} = \boldsymbol{\Psi} \boldsymbol{\sigma} + \mathbf{n} \quad (4)$$

where $\mathbf{r} = [\mathbf{r}_0^T, \dots, \mathbf{r}_{M-1}^T]^T$ is the $MN \times 1$ measurement vector, $\boldsymbol{\Psi} = [\boldsymbol{\Psi}_0^T, \dots, \boldsymbol{\Psi}_{M-1}^T]^T$ is the $MN \times Q$ dictionary matrix. Without loss of generality, the $Q \times 1$ additive noise vector \mathbf{n} is considered in Eq. (4).

3. EFFICIENT SPARSE TWR IMAGING METHOD

In this section, we propose the efficient sparse TWR imaging algorithm by combining the SPGL1 algorithm and NUFFT technique and analyze its improvements of computer memory requirement and computational complexity.

3.1. SPGL1 Algorithm

In many TWR imaging scenarios, the observed scene of interest is inherently sparse, i.e., the data may be represented with a few dominant coefficients in $\boldsymbol{\sigma}$ and others are very close to zero. As such, the sparse solution of $\boldsymbol{\sigma}$ in Eq. (4) can be obtained by utilizing the basis pursuit de-noising (BPDN) strategy

$$\hat{\boldsymbol{\sigma}} = \arg \min \|\boldsymbol{\sigma}\|_1 \quad s.t. \quad \|\mathbf{r} - \boldsymbol{\Psi} \boldsymbol{\sigma}\|_2 < \varepsilon \quad (5)$$

where $\|\cdot\|_1$ and $\|\cdot\|_2$ denote l_1 and l_2 norms, respectively. ε is the recovery error tolerance and can be determined using the cross-validation technique [12].

It is noted that the computational burden of Eq. (5) is highly dependent on the size of discretized pixels and the number of data measurements. Thus the TWR imaging problem is typically very difficult

because of the huge size of the dictionary matrix Ψ and high computational burden imposed by a fully TWR inversion algorithm. In particular, the SPGL1 software package [13] is employed to solve the BPDN problem of Eq. (5). The foremost reason for choosing SPGL1 is that it can perform BPDN method by using functional inputs for dictionary matrix Ψ instead of explicit enumeration of the dictionary matrix Ψ . The function representation of Ψ can dramatically reduce constraints in creating, storing and applying Ψ for the large-scale TWR imaging problem. Hence, the operator formalism is indispensable. The products of matrix-vector are replaced with the specially designed function handles to perform the action of Ψ and Ψ^H on arbitrary vectors.

3.2. Efficient Implementation of Operators Using NUFFT

In the SPGL1 algorithm, directly forming the matrices Ψ and Ψ^H is usually computationally infeasible due to memory limitations. Fortunately, the forward operator Ψ and the adjoint operator Ψ^H are very similar to discrete Fourier transform (DFT) matrices. In fact, Ψ and Ψ^H can be treated as type-I NUFFT and type-II NUFFT, respectively. Then the matrix-vector multiplication of two operators can be completed by NUFFT with high efficiency.

The basic idea of type-I NUFFT algorithm is to transform nonuniform samplings to uniform space data. The one-dimensional type-I NUFFT is defined as

$$F(k) = \sum_{l=0}^{L-1} f_l e^{-jkx_l}, \quad k = -\frac{K}{2}, \dots, \frac{K}{2} - 1 \quad (6)$$

where $x_l \in [0, 2\pi]$ is the ununiform space data.

Assume that $f_c = (f_0 + f_{N-1} + \Delta f)/2$. The matrix-vector multiplication of Eq. (2) can be written as

$$\begin{aligned} r_m(n + N/2) &= \sum_{q=0}^{Q-1} \sigma_q e^{-j2\pi(f_c + n\Delta f)\tau_{m,q}} \\ &= e^{-j2\pi f_c \tau_{m,q}} \sum_{q=0}^{Q-1} \sigma_q e^{-j2\pi n \Delta f \tau_{m,q}} \\ &= e^{-j2\pi f_c \tau_{m,q}} \sum_{q=0}^{Q-1} \sigma_q e^{-jn \hat{\tau}_{m,q}} \quad n = -\frac{N}{2}, \dots, \frac{N}{2} - 1 \end{aligned} \quad (7)$$

where $\hat{\tau}_{m,q} = 2\pi \Delta f \tau_{m,q}$, $r_m(n + N/2)$ is essentially the measurement data collected at the m th antenna location. It is observed that σ_q , n and $\hat{\tau}_{m,q}$ in Eq. (7) are equivalent of f_l , k and x_l in Eq. (6), respectively. Hence, Eq. (7) can be treated as the type-I NUFFT and efficiently calculated through fast Gaussian gridding-based NUFFT technique [11]. Since there are a total of M antenna locations, the forward operator Ψ can be regarded as M evaluations of type-I NUFFT.

The type-II NUFFT algorithm is used to calculate the transformation of uniform space data into ununiform space data. The one-dimensional type-II NUFFT is defined as

$$f(x_l) = \sum_{k=-\frac{K}{2}}^{\frac{K}{2}-1} F(k) e^{jkx_l} \quad l = 0, \dots, L-1 \quad (8)$$

where $F(k)$ is the uniformly sampled data, $x_l \in [0, 2\pi]$ is the ununiform space data.

The matrix-vector multiplication $\Psi_m^H \mathbf{r}_m$ can be written as

$$\begin{aligned} f(a_q) &= \sum_{n=0}^{N-1} r_m(n) \exp^{j2\pi f_n \tau_{m,q}} \\ &= \sum_{n=-N/2}^{N/2-1} r_m(n + N/2) e^{j2\pi(f_c + n\Delta f)\tau_{m,q}} \end{aligned}$$

$$\begin{aligned}
&= e^{j2\pi f_c \tau_{qm}} \cdot \sum_{n=-N/2}^{N/2-1} r_m(n + N/2) e^{jn2\pi \Delta f \tau_{m,q}} \\
&= e^{j2\pi f_c \tau_{qm}} \cdot \sum_{n=-N/2}^{N/2-1} r_m(n + N/2) e^{jn a_q} \quad q = 0, \dots, Q - 1
\end{aligned} \tag{9}$$

where $r_m(n + N/2)$ is again essentially the measurement data collected at the m th antenna position, and $a_q = 2\pi \Delta f \tau_{m,q}$ is the nonuniform space data corresponding to the m th antenna position. It is noted that $r_m(n + N/2)$, n and a_q in Eq. (9) are equivalent to $F(k)$, k and x_l in Eq. (8), respectively. Hence Eq. (9) can be regarded as type-II NUFFT and calculated with fast Gaussian gridding-based NUFFT technique. Since there are a total of M antenna locations, the adjoint operator Ψ^H involves M evaluations of type-II NUFFT.

4. SIMULATION AND EXPERIMENTAL RESULTS

4.1. Simulation Results

In this section, we evaluate the performance of the proposed imaging scheme using synthesized data. A stepped-frequency signal consisting of 200 equally spaced frequencies covering the 1 to 2.99 GHz frequency band with a frequency step of 10 MHz are used for imaging reconstruction. A monostatic synthetic line array, consisting of 51-element locations with an inter-element spacing of 2 cm is employed. Therefore the total number of the measurement data is $200 \times 51 = 10200$. A homogeneous wall of thickness 0.2 m and a dielectric constant 4 is placed in front of the array at a standoff distance of 0.5 m. As shown in Fig. 1(a), four point targets located at $(-0.64, 0.4)$ m, $(0.64, 0.4)$ m, $(-0.64, 1.6)$ m and $(0.64, 1.6)$ m with reflection coefficients all equal to 0.1 are considered in the sparse scene. The region to be imaged is chosen to be 2 m (crossrange) \times 2 m (downrange) and divided into $50 \times 50 = 2500$ pixels. Additive complex white Gaussian noise is added to the measurement data with a signal-to-noise ratio (SNR) of 10 dB. The wall reflection is assumed to be removed by subtracting the empty scene measurements from the measurement with targets. Numerical experiments are implemented on a desktop with Intel(R) Core(TM) i5-3470U CPU at 3.2 GHz with an 8 GB memory with MATLAB platform.

For the traditional SPGL1 imaging algorithm, the dictionary matrix has a size of $10200 \times 2500 = 25500000$. A double-precision floating point variable is kept in memory by 8 bytes. Each element of the dictionary matrix is a complex number and requires 16 bytes in memory. This means that nearly 389 MB data memory is required for the storage of the dictionary matrix. However, for the NUFFT-based SPGL1 imaging algorithm, only the two-way traveling time of each pixel for 51 monostatic antenna locations should be calculated offline and stored in the memory. There are a total of $51 \times 2500 = 127500$ time delays to be calculated and thus only a total of 0.97 MB computer memory is required for the storage of the values of time delays. Since the memory requirements of the NUFFT-based SPGL1 has no relationship with the number of transmitted frequencies, the memory requirement of the NUFFT-based algorithm is much less than that of the conventional SPGL1 algorithm. Figs. 1(b) and (c) respectively report the reconstruction results obtained by means of the conventional SPGL1 algorithm and NUFFT-based SPGL1 imaging algorithm. The true target positions are indicated with black rectangles. It is observed that the imaging result of the proposed NUFFT-based SPGL1 imaging method is as good as that with the conventional SPGL1 imaging method. The total running time of the traditional and NUFFT-based SPGL1 imaging method is 2.6 s and 2.2 s, respectively.

In order to provide a quantitative analysis of the reconstruction accuracy of the proposed imaging method, we define the normalized mean squared error (NMSE) as

$$\text{NMSE} = \|\hat{\mathbf{f}} - \mathbf{f}\|_2^2 / \|\mathbf{f}\|_2^2 \tag{10}$$

where $\hat{\mathbf{f}}$ is a column vector, and each element of $\hat{\mathbf{f}}$ represents the value of each pixel of the reconstructed imaging result. \mathbf{f} is also a column vector with each element denoting the value of each pixel of original scene. The NMSE for the traditional SPGL1 and NUFFT-based SPGL1 imaging results versus different

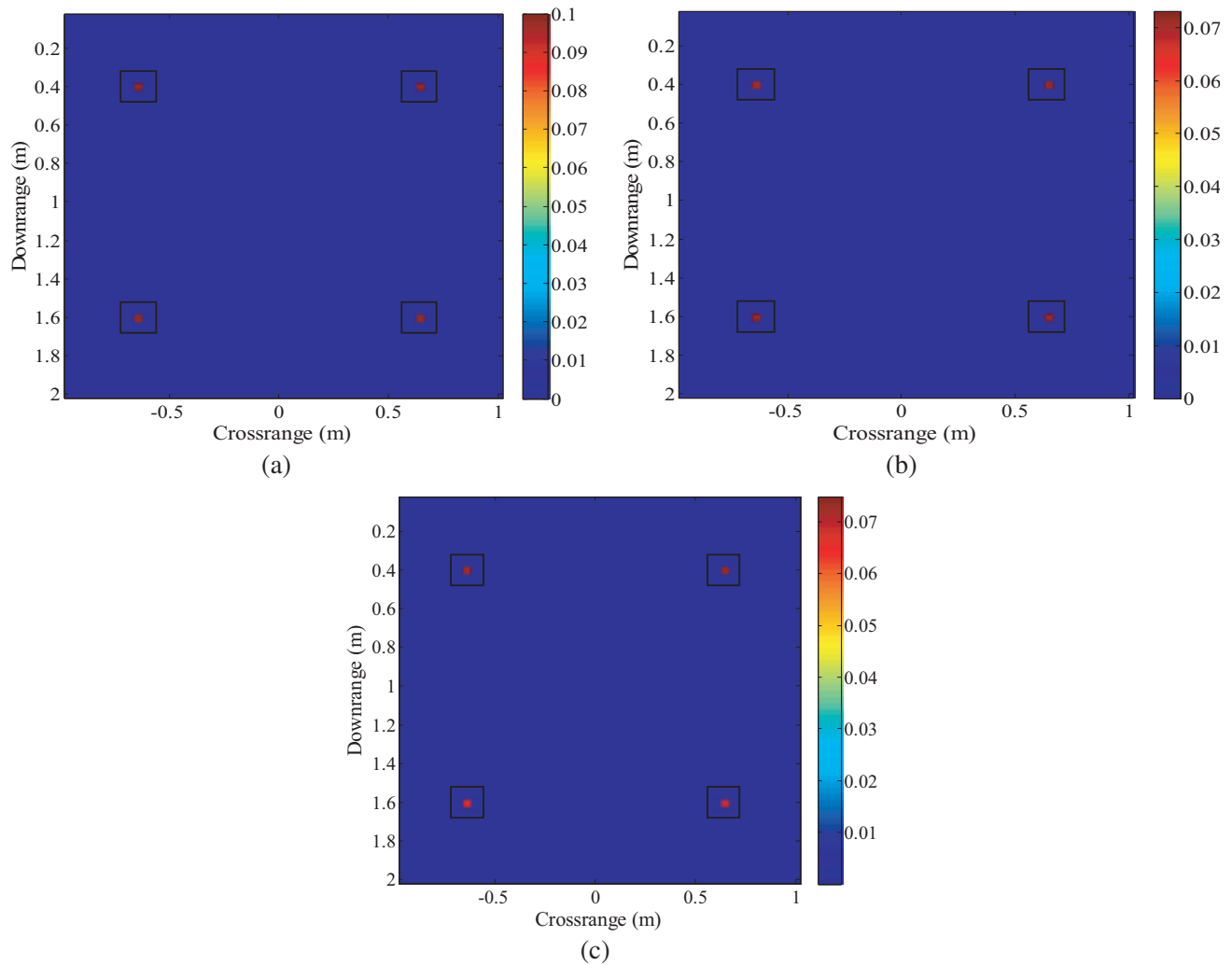


Figure 1. (a) Geometry of the original scenario. (b) Imaging result with the traditional SPGL1 algorithm. (c) Imaging result with the NUFFT-based SPGL1 algorithm.

SNR levels are provided in Fig. 2, where results are computed as the mean of NMSE from 30 independent experiments. It can be seen that the NMSE decreases as the SNR increases. Furthermore, the NMSE of the proposed NUFFT-based SPGL1 imaging method is relatively larger than that of the conventional SPGL1 imaging method. This phenomenon is essentially caused by a few sidelobes in the imaging result introduced by the calculation approximation error of NUFFT.

To compare the memory performance of the classical SPGL1 and the proposed NUFFT-based imaging method, the number of discretized pixels is changed, and the required computer memories for two imaging methods are compared. Fig. 3 gives the memory requirement of two imaging methods as a function of the number of discretized pixels. It is observed that increasing the number of pixels increases memory requirement of two imaging methods. Moreover, the proposed NUFFT-based SPGL1 imaging method requires much less memory compared to the traditional SPGL1 imaging method and is practical for large-scale TWR imaging applications. When the total number of pixels increases to $2500 \cdot 2^4 = 40000$, the required memory of NUFFT-based SPGL1 algorithm is nearly 1/446 times that of the traditional SPGL1 algorithm.

Another advantage of the proposed imaging method is the computational efficiency. The running time consumed by the conventional and proposed SPGL1 imaging algorithm against the number of discretized pixels are shown in Fig. 4, where each value is evaluated based on the average of 10 trials.

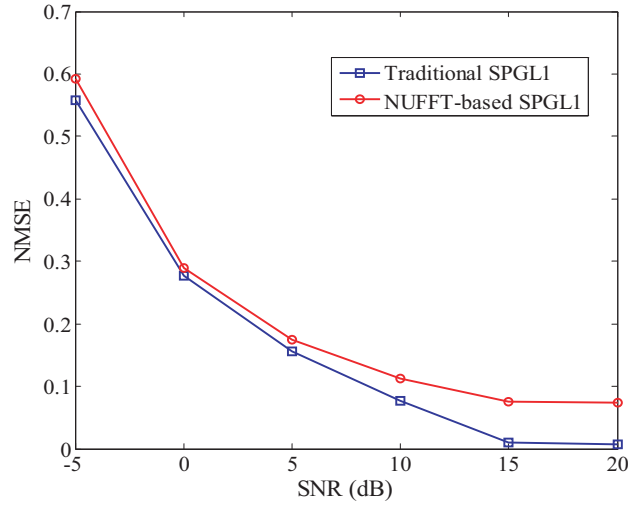


Figure 2. NMSE comparison of two imaging methods under different SNR values.

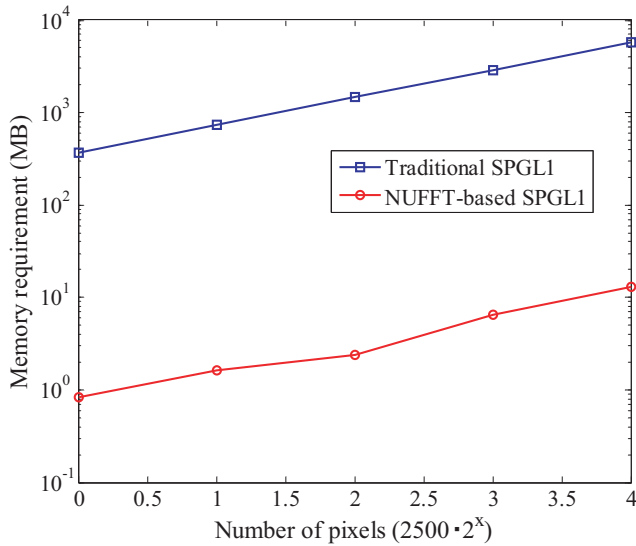


Figure 3. Memory requirement comparison of two imaging methods.

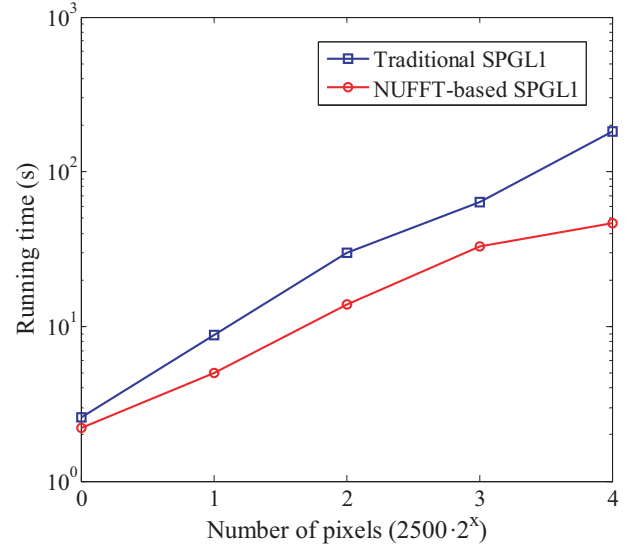


Figure 4. Running time comparison of two imaging methods.

Benefiting from the computational efficiency of NUFFT for matrix-vector multiplication, the proposed NUFFT-based SPGL1 imaging method is much faster than the traditional imaging method, especially when the number of discretized pixels is relatively large. When the total number of pixels increases to $2500 \cdot 2^4 = 40000$, the speed up ratio approaches nearly 4.

4.2. Experimental Results

The proposed NUFFT-based SPGL1 sparse imaging method is evaluated on the experimental TWR data collected in the Radar Imaging Lab of the Center for Advanced Communications at Villanova University. The wall is built from a wooden frame, which is fasten with 0.019 m plywood on one side and 0.016 m gypsum wallboard on the other side. A 69-element linear array of length 1.5 m is synthesized with an inter-element spacing of 0.022 m, and a stepped-frequency signal of 1 GHz bandwidth centered at 2.5 GHz with a frequency step size of 5 MHz is used to image the scene. The nonhomogeneous wall

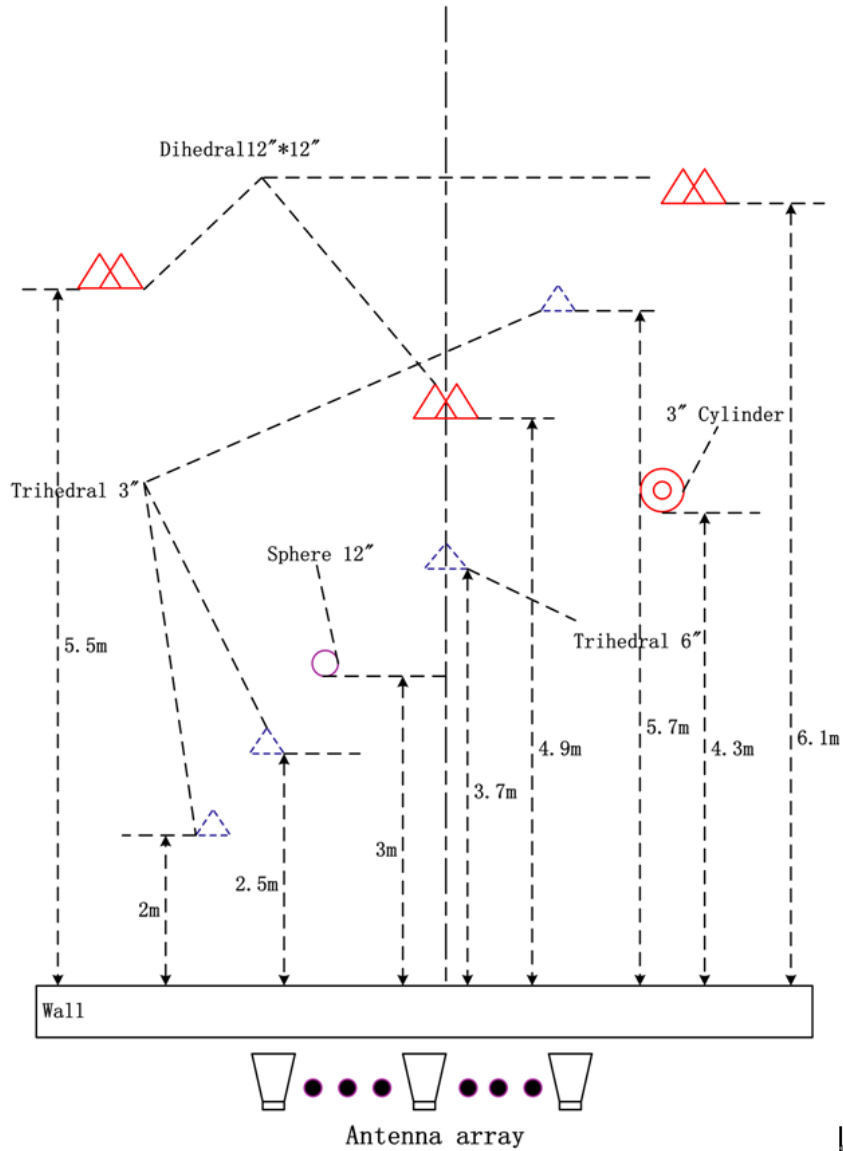


Figure 5. Ground-truth of the observed scene.

has a thickness of 0.127 m and is placed at a standoff distance of 0.0127 m from the front face of the antennas. More detailed information about the experimental setup is provided in [14]. The scene to be imaged consists of nine targets: a sphere, three dihedrals, four trihedrals and a cylinder. Fig. 5 shows the true positions of nine targets in the observed scene. The imaged scene is chosen to have a downrange of [1, 7] m and a crossrange of [-2, 2] m and divided into 121×81 spatial grids with an interval of 0.05 m in both downrange and crossrange. At each measurement position, 200 frequency measurements ranging from 2 GHz to 2.995 GHz with a step of 5 MHz are utilized for imaging reconstruction. In addition, background subtraction is performed on the raw data to remove the strong wall reflection signal.

The imaging reconstruction results of the experimental data using two imaging methods are illustrated in Fig. 6. The true target locations are indicated by the black rectangles. It is observed from Fig. 6 that both the traditional and NUFFT-based SPGL1 sparse imaging methods can accurately detect and locate eight targets. Due to its weak return with very low SNR, the small trihedral at a downrange of 5.7 m is missed in both Fig. 6(a) and Fig. 6(b). The imaging results also indicate that the NUFFT-based SPGL1 imaging method can also reconstruct the real data image as the standard SPGL1 imaging method with nearly the same quality. However, while the traditional SPGL1 imaging method

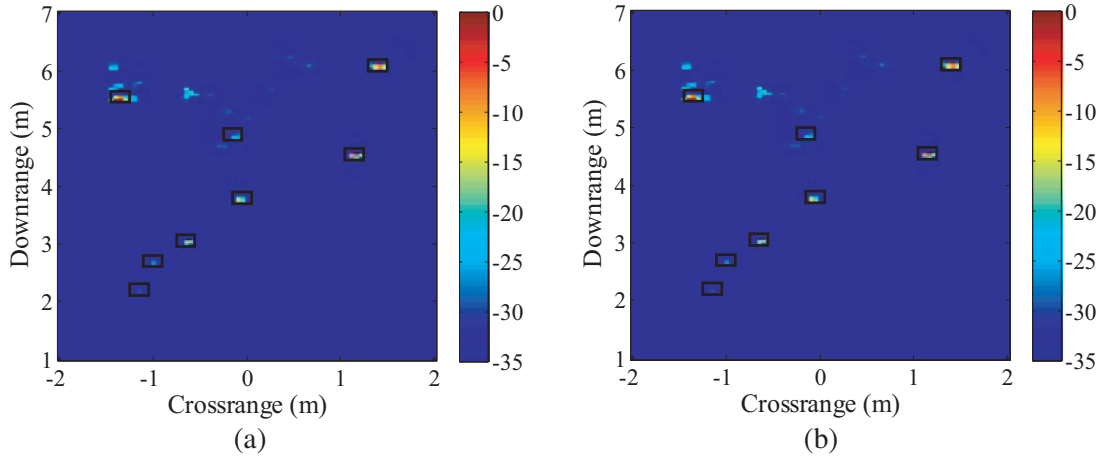


Figure 6. Imaging results of experimental data. (a) Imaging result by the traditional SPGL1 algorithm. (b) Imaging result by the NUFFT-based SPGL1 algorithm.

requires a memory of 1.92 GB and takes 9.6s to generate its imaging result, the proposed NUFFT-based imaging method only requires a computer memory of 4.7MB and takes 5.4s to achieve image reconstruction. It is concluded that the proposed NUFFT-based imaging method can dramatically reduce the required computer memory and improve the computational efficiency. Thus it can be a good candidate algorithm for imaging the large investigated area or on-site imaging applications.

5. CONCLUSION

In this paper, we have proposed an efficient sparse TWR imaging algorithm which combines the SPGL1 algorithm and NUFFT technique. The simulated and experimental results have shown that compared with the conventional SPGL1 sparse imaging reconstruction algorithm, the proposed sparse imaging method can significantly reduce the required computer memory and computational cost, and achieve similar recovered image quality. Hence the proposed NUFFT-based SPGL1 sparse imaging method is more practical for large-scale TWR imaging applications.

ACKNOWLEDGMENT

The authors would like to thank the Center for Advanced Communications at Villanova University for providing the experimental TWR data. This work was supported by the National Natural Science Foundation of China under Grant 61671310 and 61302172, and the Aeronautical Science Foundation of China under Grant 2016ZC54013.

REFERENCES

1. Amin, M., Ed., *Through-the-wall Radar Imaging*, CRC Press, Boca Raton, FL, USA, 2011.
2. Yoon, Y.-S. and M. G. Amin, "Compressed sensing technique for high-resolution radar imaging," *Proc. SPIE*, Vol. 6968, 69681A-1–69681A-10, 2008.
3. Huang, Q., L. Qu, B. Wu, and G. Fang, "UWB through-wall imaging based on compressive sensing," *IEEE Trans. Geosci. Remote Sens.*, Vol. 48, No. 3, 1408–1415, Mar. 2010.
4. Browne, K. E., R. J. Burkholder, and J. L. Volakis, "Fast optimization of through-wall radar images via the method of Lagrange multipliers," *IEEE Trans. Antennas Propag.*, Vol. 61, No. 1, 320–328, Jan. 2013.

5. Li, G. and R. Burkholder, "Hybrid matching pursuit for distributed through-wall radar imaging," *IEEE Trans. Antennas Propag.*, Vol. 63, No. 4, 1701–1711, Apr. 2015.
6. Zhang, W. and A. Hoofar, "A generalized approach for SAR and MIMO radar imaging of building interior targets with compressive sensing," *IEEE Antennas Wireless Propag. Lett.*, Vol. 14, 1052–1055, 2015.
7. Lagunas, E., M. G. Amin, F. Ahmad, and M. Nájjar, "Joint wall mitigation and compressive sensing for indoor image reconstruction," *IEEE Trans. Geosci. Remote Sens.*, Vol. 51, No. 2, 891–906, Feb. 2013.
8. Ahmad, F., J. Qian, and M. G. Amin, "Wall clutter mitigation using discrete prolate spheroidal sequences for sparse reconstruction of indoor stationary scenes," *IEEE Trans. Geosci. Remote Sens.*, Vol. 53, No. 3, 1549–1557, Mar. 2015.
9. Leigsnering, M., F. Ahmad, M. Amin, and A. Zoubir, "Parametric dictionary learning for sparsity-based TWRI in multipath environments," *IEEE Trans. Aerosp. Electron. Syst.*, Vol. 52, No. 2, 532–547, Apr. 2016.
10. Van den Berg, E. and M. P. Friedlander, "Probing the Pareto frontier for basis pursuit solutions," *SIAM J. Sci. Comput.*, Vol. 31, 890–912, Nov. 2008.
11. Greengard, L. and J.-Y. Lee, "Accelerating the nonuniform fast Fourier transform," *SIAM Rev.*, Vol. 46, No. 3, 443–454, 2004.
12. Ward, R., "Compressed sensing with cross validation," *IEEE Trans. Inf. Theory*, Vol. 55, No. 12, 5773–5782, Dec. 2009.
13. Van den Berg, E. and M. P. Friedlander, "SPGL1: A solver for large-scale sparse reconstruction," Jun. 2007, [Online], Available: <http://www.cs.ubc.ca/labs/scl/spgl1>.
14. Dilsavor, R., et al., "Experiments on wideband through the wall imaging," *Proc. SPIE Symp. Defense Security, Algorithms Synthetic Aperture Radar Imagery XII Conf.*, Vol. 5808, 196–209, 2005.